2-2018

Real-Time Variable Multidelay Controller for Multihazard Mitigation

Liang Cao
Iowa State University, liangcao@iastate.edu

Simon Laflamme
Iowa State University, laflamme@iastate.edu

Real-Time Variable Multidelay Controller for Multihazard Mitigation

Abstract
High performance control systems (HPCS), including semiactive, active, and hybrid damping systems, are effective solutions to increase structural performance versus multihazard excitations. However, the implementation of HPCS within structural systems is still in its infancy, because of the complexity in designing a robust closed-loop control system that can ensure reliable and high mitigation performance. To overcome this challenge, a new type of controller with high adaptive capabilities is proposed. The control algorithm is based on real-time embedding of measurements to minimally represent the essential dynamics of the controlled system, therefore providing adaptive input space capabilities. This type of controller is termed an input-space dependent controller. In this paper, a specialized case of input-space dependent controller is investigated, where the embedding dimension is fixed, but the time delay used in the construction of the embedding varies with time. This constitutes a variable multidelay controller (VMDC), which includes an algorithm enabling the online selection of a time delay based on information theory. Here, optimal time delay selection is first studied and its applicability of the VMDC algorithm demonstrated. Numerical simulations are conducted on a single-degree-of-freedom (SDOF) system to study the performance of the VMDC versus different control strategies. Results show a significant gain in performance from the inclusion of an adaptive input space, and that the algorithm was robust with respect to noise. Simulations also demonstrate that critical gains in performance could be obtained from added knowledge in the system's dynamics by comparing mitigation results with a linear quadratic regulator (LQR) controller. Additional simulations are conducted on a three degrees-of-freedom (3DOF) system, which consists of a model structure equipped with an actuator and subjected to nonsimultaneous multihazards. Results show enhanced mitigation performance of the VMDC versus LQR strategies when using limited-state feedback, validating the capability of the controller at mitigating vibrations based on limited knowledge and limited measurements, and thus its promise at multihazard applications.

Keywords
Input-space dependent controller, Data driven controller, Embedding theorem, Multidelay, Multihazard, Structural control, Real-time, Adaptive control

Disciplines
Civil and Environmental Engineering | Controls and Control Theory | Structural Engineering

Comments
This is a manuscript of an article published as Cao, Liang, and Simon Laflamme. "Real-Time Variable Multidelay Controller for Multihazard Mitigation." Journal of Engineering Mechanics 144, no. 2 (2017): 04017174. DOI: 10.1061/(ASCE)EM.1943-7889.0001406. Posted with permission.

Real-Time Variable Multi-Delay Controller for Multi-Hazard Mitigation

Liang Cao, A.M. ASCE [1]; Simon Laflamme, A.M. ASCE [2]

ABSTRACT

High performance control systems (HPCS), including semi-active, active and hybrid damping systems, are effective solutions to increase structural performance versus multi-hazard excitations. However, the implementation of HPCS within structural systems is still in its infancy, because of the complexity in designing a robust closed-loop control system that can ensure reliable and high mitigation performance. To overcome this challenge, a new type of controller with high adaptive capabilities is proposed. The control algorithm is based on real-time embedding of measurements to minimally represent the essential dynamics of the controlled system, therefore providing adaptive input space capabilities. This type of controller is termed input-space dependent controller. In this paper, a specialized case of input-space dependent controller is investigated, where the embedding dimension is fixed, but the time delay used in the construction of the embedding varies with time. This constitutes a variable multi-delay controller (VMDC), which includes an algorithm enabling the online selection of a time delay based on information theory. Here, optimal time delay selection is first studied and its applicability of the VMDC algorithm demonstrated. Numerical simulations are conducted on a single-degree-of-freedom system to study the performance of the VMDC versus different control strategies. Results show a significant gain in performance from the inclusion of an adaptive input space, and that the algorithm was robust with respect to noise. Simulations also demonstrate that critical gains in performance could be obtained from added knowledge in the system's dynamics by comparing mitigation results with a linear quadratic regulator (LQR) controller. Additional simulations are conducted on a three degrees-of-freedom system, which consists of a model structure equipped with an actuator and subjected to non-simultaneous multi-hazards. Results show enhanced mitigation performance of the VMDC versus LQR strategies when using limited-state feedback, validating the capability of the controller at mitigating vibrations based on limited knowledge and limited measurements, and thus its promise at multi-hazard applications.

Keywords: input-space dependent controller, data driven controller, embedding theorem, multi-delay, multi-hazard, structural control, real-time, adaptive control

INTRODUCTION

High performance control systems (HPCS), including active (Ubertini 2008; Materazzi and Ubertini 2012; Venanzi et al. 2013), semi-active (Cao et al. 2015; Amjadian and Agrawal 2017) and hybrid damping systems (Yang and

[1]Postdoctoral Research Associate, Department of Civil, Construction, and Environmental Engineering, Iowa State University, Ames, IA, 50011, corresponding author; email:liangcao@iastate.edu.

[2]Associate Professor, Department of Civil, Construction, and Environmental Engineering, and Department of Electrical and Computer Engineering, Iowa State University, Ames, IA, 50011.

Agrawal 2002; Love et al. 2011), have gained popularity in the field of structural control. The damping force of HPCS can be varied in order to provide better performance under various types of excitations. It follows that HPCS can be applied over a broad range of excitation bandwidths (Connor and Laflamme 2014; Ubertini and Materazzi 2013; Cao et al. 2016). However, the implementation of HPCS is challenged by the complexity in designing a robust close-loop control system that is capable of ensuring robust and high mitigation performance, in particular under multi-hazard excitations (e.g., extreme wind events, earthquake, hurricanes). Obstacles in designing an HPCS controller for multi-hazard mitigation include: 1) uncertainties on dynamic parameters are very large, and excitations are unknown and varying over a large frequency bandwidth, in particular for a multi-hazard framework; 2) non-negligible probabilities of failure of sensors over time and limited available measurements; 3) requirement on the control system to perform immediately as designed; and 4) unavailability of input-output data sets during design for the tuning of paramters (Laflamme et al. 2012a; Zou et al. 2015).

Several controllers have been proposed in literature to cope with these structural control challenges. Model-driven controllers (MDCs), including linear quadratic regulators (LQR) and Lyapunov controllers, have been widely researched. These controllers require some level of knowledge about the system and may provide sub-optimal performance when dynamic parameters are inaccurate or unknown (Anderson et al. 2005; Anderson and Dehghani 2008). Data driven controllers (DDCs) overcome this drawback since they only rely on implicit information from measurements. Typical DDCs include SPSA-based (Simultaneous Perturbation Stochastic Approximation) data driven control (Spall 2009), model-free adaptive controllers (Hou and Jin 2011), neurocontrollers (Lee et al. 2006; Laflamme and Connor 2009; Laflamme et al. 2011), virtual reference feedback tuning (Campestrini et al. 2011), unfalsified control(Van Helvoort et al. 2007), and fuzzy controllers (Li et al. 2012).

Of particular interest are DDCs based on time delay observation feedback in the form

$$\begin{aligned} u(t) &= \sum_{i=1}^{d} g_i y(t-(i-1)\tau) \\ &= \mathbf{G}^T \boldsymbol{\nu} \end{aligned} \tag{1}$$

where u is the control force varying as a function of time t, y is an observation or input, τ is the time delay, d is the number of delays, and $\boldsymbol{\nu} \in \mathbb{R}^{d\times 1}$ is the delay vector, g and $\mathbf{G} \in \mathbb{R}^{d\times 1}$ are the control gains and the control gain matrix, respectively. An advantage of utilizing a time delay feedback is the capability of providing control feedback based on limited and local measurements (e.g., using a single sensor).

A critical challenge in designing time delay controllers is in the selection of the optimal τ and d that can properly represent essential dynamics in the delay vector $\boldsymbol{\nu}$. Optimal values for τ and d may vary as a function of time, in particular when the excitation is nonstationary (e.g., multi-hazard excitations). In previous work, the authors have

proposed a new control strategy, termed input space dependent controller (ISDC), where the controller's parameters (e.g., time delay τ, size of delays d and control gains g) can be selected and sequentially adapted. The principle of the ISDC is based on the Embedding Theorem (Takens 1981; Stark 1999; Stark et al. 2003). From this theorem, there exists an optimal delay vector $v^*(\tau^*, d^*)$ that contains system's essential dynamics, where the asterisk denotes an optimal value. The ISDC is to seek τ^* and d^* from the inputs, where the term "input-space dependent", and uses these values to constitute the control rule (Eq. (1)).

The Embedding Theorem was first developed for autonomous systems (Takens 1981), and further developed for nonautonomous systems with deterministic forcing (Stark 1999), stochastic forcing (Stark et al. 2003), and state-dependent forcing (Caballero 2000). It has also been shown that v can be modified to include unknown inputs and multivariate observations (Monroig et al. 2009).The Embedding Theorem has been used in several engineering applications, including structural control (Li and Peng 2007; Da Silva et al. 2008; Tikka 2009; Zolock and Greif 2009; Laflamme et al. 2012a) and structural health monitoring(Moniz et al. 2005; Overbey et al. 2007; Monroig et al. 2009). To the best knowledge of the authors, never the online selection of τ and d has been addressed, nor the idea of a time-varying architecture of the delay vector applied.

In this paper, we investigate the specific case of a time-varying $\tau(t)$, letting d constant, forming a specialized ISDC-type controller termed Variable Multi-Delay Controller (VMDC). Previous analytical results in Refs. (Cao and Laflamme 2016a; Cao and Laflamme 2016b) are presented to introduce the principle of the time delay selection method. After, a new sequential adaptive VMDC algorithm is proposed that includes a real-time adaptive rule for $\tau(t)$ and $\mathbf{G}(t)$. The new development presented in this paper lead to the new adaptive VMDC algorithm. While the study of a time-varying formulation for d is left to future work, the algorithm developed in what follows is applicable to any embedding dimension d.

The paper is organized as follows. The next section presents previous results on the online selection rule of optimal time delay τ^*. A time delay selection method based on information theory is presented. This method is derived from the analytical solution for a single degree-of-freedom (SDOF) system minimizing a transfer function, followed by a comparison with an analytical solution obtained based on information theory. The subsequent section presents the VMDC algorithm, which includes the new adaptive time delay strategy along with adaptive control gains to ensure stability. It is followed by parametric studies to investigate the performance of the proposed VMDC under different types of excitation, including a comparison with different controllers (MDCs and DDCs). After, numerical simulations on a three story structure model subjected to ground motion are conducted to demonstrate structural control applications. The last section concludes the paper.

OPTIMAL TIME DELAY SELECTION

In this section, we study the opportunity of using the Embedding Theorem for selecting the controller's input

parameter τ. Consider an SDOF system of the form

$$m\ddot{x}(t) + c\dot{x}(t) + kx(t) = f(t) + u(t) \tag{2}$$

where m, c and k are the system's mass, damping and stiffness, respectively, $x(t)$ is the displacement, $u(t)$ is the control force from Eq. (1), $f(t)$ is an external excitation and the dot denotes the time derivative. For simplicity, take the observation feedback $y(t)$ (Eq. (1)) as equal to the displacement state $x(t)$. The Embedding Theorem states that the topological space of unknown system can be reconstructed from a properly built delay vector v^* using limited observations $y(t)$, where v^*, contains the essential dynamics of the system. It is hypothesized that v^* can be used as an optimized input space to the DDC, because it constitutes a good representation of the system under control, resulting in an efficient representation for the controller.

The analytical solution for an SDOF system subjected to a harmonic forcing and controlled with a fixed time delay and constant $d = 2$ is first derived in the next subsection. The fixed embedding dimension $d = 2$ is used since it is sufficient to embed the system's response when subjected to harmonic loading (Kennel et al. 1992). The objective is to seek the optimal time delay τ^* that can provide the best performance for the SDOF system. After, a new method for selecting τ^* based on information theory is proposed, and its analytical solution for a harmonic excitation is derived and compared.

Optimal Time Delay - SDOF Analytical Solution

Consider the following control rule in the SDOF from Eq. (2):

$$u(t) = -g_1 x(t) - g_2 x(t-\tau) \tag{3}$$

where g_1 and g_2 are control gains. Taking the transformations $\rho_{g1} = g_1/k$ and $\rho_{g2} = g_2/k$:

$$\ddot{x}(t) + 2\xi\,\omega_n \dot{x}(t) + \omega_n^2 x(t) = -\rho_{g1}\,\omega_n^2 x(t) - \rho_{g2}\omega_n^2 x(t-\tau) + f(t)/m \tag{4}$$

where $\xi = \frac{c}{2m\omega_n}$ and $\omega_n = \sqrt{k/m}$ are the fundamental damping ratio and natural frequency of the system, respectively.

The harmonic excitation $f(t)$ in Eq. (4) has the form

$$f(t) = \hat{f}\sin(\Omega t) \tag{5}$$

where Ω and $\hat{f}$ are the frequency and magnitude of the harmonic excitation, respectively. The vibration response of the SDOF system can be expressed in the form

$$x(t) = A\sin(\Omega t) + B\cos(\Omega t) \tag{6}$$

with

$$\begin{cases} -A\Omega^2 - 2\xi\,\omega_n\Omega B + \omega_n^2 A + \rho_{g1}\omega_n^2 A + \rho_{g2}\omega_n^2(A\cos\tau\Omega + B\sin\tau\Omega) = \frac{\hat{f}}{m} \\ -B\Omega^2 + 2\xi\,\omega_n\Omega A + \omega_n^2 B + \rho_{g1}\omega_n^2 B + \rho_{g2}\omega_n^2(B\cos\tau\Omega - A\sin\tau\Omega) = 0 \end{cases} \tag{7}$$

A transfer function $H = |\max(x(t)) \cdot k/\hat{f}|$ can be obtained by solving A and B in Eq. (7) and substituting back in Eq. (6)

$$H = \frac{1}{\sqrt{[1-\rho^2+\rho_{g1}+\rho_{g2}\cos(2\pi\rho_\tau)]^2 + [\rho_{g2}\sin(2\pi\rho_\tau) - 2\xi\rho]^2}} \tag{8}$$

The transfer function H versus $\rho = \Omega/\omega_n$ under various values of ρ_τ, where $\rho_\tau = \tau/T$, is plotted in Fig. 1. The figure is produced taking $\rho_{g1} = 2$ and $\rho_{g2} = -1$, and $\rho_\tau \leq 0.25$. The time delay ratio ρ_τ is limited to 0.25 since any additional delay would provide redundant information in terms of topology of the phase-space for a harmonic excitation. Results demonstrate that H decreases as ρ_τ increases until a critical frequency ratio ρ_{cr} is reached. The value of ρ_{cr} can be calculated by substituting appropriate values for ρ_τ in Eq. (8)

$$\rho_{cr} = \xi + \sqrt{\xi^2 + \rho_{g1} + 1} \tag{9}$$

The optimal time delay for a harmonic excitation of different frequencies can be obtained by comparing values of H with various time delay ratio ρ_τ. However, a stability analysis needs first to be conducted to bound ρ_τ, ρ_{g1}, and ρ_{g2}.

Stability Analysis

To conduct the stability analysis, the homogeneous solution for Eq. (6) is expressed in the form $x(t) = \hat{x}e^{\lambda t}$, where $\hat{x}$ is an amplitude, yielding the characteristic equation

$$\lambda^2 + 2\xi\,\omega_n\lambda + \omega_n^2 + \rho_{g1}\omega_n^2 + \rho_{g2}\omega_n^2 e^{-\tau\lambda} = 0 \tag{10}$$

The last exponential term can be expressed by the a power series

$$e^{-\tau\lambda} = 1 - \tau\lambda + \frac{1}{2}(\tau\lambda)^2 - \frac{1}{6}(\tau\lambda)^3 + ... \tag{11}$$

Retaining the first two terms and neglecting the higher order terms, equation (10) becomes

$$\lambda^2 + (2\xi\omega_n - \rho_{g2}\omega_n^2\tau)\lambda + \omega_n^2 + \rho_{g1}\omega_n^2 + \rho_{g2}\omega_n^2 = 0 \tag{12}$$

Two complex roots $\lambda_R \pm \lambda_I i$ of λ can be estimated as

$$\begin{aligned} \lambda_R &= -\xi\omega_n + \frac{1}{2}\rho_{g2}\omega_n^2\tau \\ \lambda_I &= \frac{1}{2}\omega_n\sqrt{4 + 4\rho_{kg1} + 4\rho_{g2} - (2\xi - \rho_{g2}\omega_n\tau)^2} \end{aligned} \tag{13}$$

Stability requires $\lambda_R < 0$, which gives an expression for ρ_{g2}

$$\rho_{g2} < 2\xi/(\omega_n\tau) \tag{14}$$

Also, if λ has two real numbers as roots, the imaginary part vanishes and λ becomes

$$\lambda = -\xi\omega_n + \frac{1}{2}\rho_{g2}\omega_n^2\tau \pm \frac{1}{2}\omega_n\sqrt{(2\xi - \rho_{g2}\omega_n\tau)^2 - 4\rho_{g1} - 4\rho_{g2} - 4} \tag{15}$$

The maximum root of λ must be negative for $\lambda < 0$, yielding

$$1 + \rho_{g1} + \rho_{g2} > 0 \tag{16}$$

The stability criterions for control gains g_1 and g_2 can be established based on Eqs. (14) and (16). In addition, the exponential term in Eq. (10) can be expanded to investigate the stability of τ in terms of ρ_{g1} and ρ_{g2}

$$e^{-\tau\lambda} = \frac{1 - \frac{1}{2}\tau\lambda}{1 + \frac{1}{2}\tau\lambda} + O[(\tau\lambda)^3] \tag{17}$$

which yields a third degree polynomial in λ

$$\tau\lambda^3 + (2 + 2\xi\omega_n\tau)\lambda^2 + (4\xi\omega_n + \omega_n^2\tau + \rho_{g1}\omega_n^2\tau - \rho_{g2}\omega_n^2\tau)\lambda + 2\omega_n^2 + 2\rho_{g1}\omega_n^2 + 2\rho_{g2}\omega_n^2 = 0 \tag{18}$$

A stability plot under various feedback coefficients ($\rho_{g1} = 1$ and $\rho_{g2} = \{-0.1, -0.2, -0.3, -0.4, -0.5\}$) is generated using Eq. (18), shown in Fig. 2. The SDOF system has a natural period $T = 2$ sec and a fundamental damping

ratio $\xi = 2\%$ typical of a civil structure. Specific values for ρ_{g1} and ρ_{g2} were selected to meet stability criterions from Eqs. (14) and (16). The bound on time delay to ensure stability under varying ρ_{g2} is shown in Fig. 2. The path of λ moves from the left half-plane to the right half-plane as time delay τ increases. The maximum time delay for various ρ_{g2} corresponds to $\lambda_R = 0$ or $\lambda = \lambda_I i$. Substituting for λ in Eq. (10) leads to

$$-\lambda_I^2 + \omega_n^2 + \rho_{g1}\omega_n^2 + \rho_{g2}\omega_n^2 \cos(\tau\lambda_I) + (2\xi\omega_n\lambda_I - \rho_{g2}\omega_n^2 \sin(\tau\lambda_I))i = 0 \tag{19}$$

Eq. (19) is satisfied when the real and imaginary terms vanish:

$$\begin{aligned} -\lambda_I^2 + \omega_n^2 + \rho_{g1}\omega_n^2 + \rho_{g2}\omega_n^2 \cos(\tau\lambda_I) = 0 \\ 2\xi\omega_n\lambda_I - \rho_{g2}\omega_n^2 \sin(\tau\lambda_I) = 0 \end{aligned} \tag{20}$$

giving

$$\lambda_I^4 + (4\xi^2\omega_n^2 - 2\omega_n^2 - 2\rho_{g1}\omega_n^2)\lambda_I^2 + (\omega_n^2 + \rho_{g1}\omega_n^2)^2 - \rho_{g2}^2\omega_n^4 = 0 \tag{21}$$

The roots of Eq.(21) are given by

$$\lambda_I = \pm\sqrt{\omega_n^2 + \rho_{g1}\omega_n^2 - 2\xi^2\omega_n^2 \pm \frac{1}{2}\sqrt{16\xi^4\omega_n^4 - 16\xi^2\omega_n^4 - 16\xi^2\rho_{g1}\omega_n^4 + 4\rho_{g2}^2\omega_n^4}} \tag{22}$$

A stability condition independent on time delay can be obtained from Eq. (21). Such stability is guaranteed if λ_I has complex roots or the solution for λ has no imaginary part. This occurs when

$$\rho_{g2}^2 - 4\xi^2\rho_{g1} < 4\xi^2 - 4\xi^4 \tag{23}$$

In the delay dependent region, only the two positive roots of λ_I need to be investigated because the maximum allowable time delay corresponds to $\pm\lambda_I i$. By solving the first part of Eq. (20) for τ in terms of λ_I, the maximum allowable time delay $\tau|_{\max}$ can be calculated and taken as the minimum positive value

$$\tau|_{\max} = \frac{1}{\lambda_I}\cos^{-1}\left(\frac{-\rho_{g1}\omega_n^2 - \omega_n^2 + \lambda_I^2}{\rho_{g2}\omega_n^2}\right) \tag{24}$$

Figure 3 plots $\tau|_{\max}$ versus ρ_{g2} for $T_n = 2$ s ,$\xi = 2\%$ under various values of ρ_{g1}. Values for ρ_{g1} and ρ_{g2} are selected to meet the stability criterions on control gains. Results show that $\tau|_{\max}$ decreases as ρ_{g1} increases, and varying ρ_{g2} will influence $\tau|_{\max}$.

In summary, three stability conditions can be established:

1. $\rho_{g2} < 2\xi/(\omega_n \tau)$
2. $1 + \rho_{g1} + \rho_{g2} > 0$
3. $\tau|_{\max} = \frac{1}{\lambda_I} \cos^{-1}\left(\frac{-\rho_{g1}\omega_n^2 - \omega_n^2 + \lambda_I^2}{\rho_{g2}\omega_n^2}\right)$

The optimal time delay τ^* can be calculated as a function of ρ by combining the stability conditions and H function results (Fig. 1). The optimal time delay ratio ρ_{τ^*} under different frequency inputs for $\rho_{g1} = 2$ and $\rho_{g2} = -1$ is plotted in Fig. 4. The value of τ^* is bounded by the stability condition limit (red line; $\rho_{\tau^*} = \tau|_{\max}/T$) until it reaches the optimal value obtained from H function results (black dashed line, $\rho_{\tau^*} = \tau^*/T$). Once the excitation ratio ρ is higher than the critical frequency ratio ρ_{cr} (Eq. 9), no time delay (blue dashed-dotted line, $\rho_{\tau^*} = 0$) yields the best performance.

Optimal Time Delay - Information Theory

The procedure to select τ^* in the proposed VMDC is to conduct the mutual information (MI) test (Fraser and Swinney 1986) based on Shannon's information theory. The MI test is used to measure the level of relevant information from the past observations contained in the current observations. Take two sets of measurements f_1 and f_2. The MI between f_1 and f_2 can be expressed as

$$\begin{aligned} \mathrm{MI}(f_1, f_2) = &- \sum_{i=1}^{n} \mathrm{p}(f_{1i}) \log_2 \mathrm{p}(f_{1i}) - \sum_{j=1}^{n} \mathrm{p}(f_{2j}) \log_2 \mathrm{p}(f_{2j}) \\ &+ \sum_{i=1}^{n} \sum_{j=1}^{n} \mathrm{p}(f_{1i} f_{2j}) \log_2 \mathrm{p}(f_{1i} f_{2j}) \end{aligned} \tag{25}$$

over n measurements. The first local minima in MI indicates that a high level of new information is contained in the new observations, and is therefore taken as τ^*. There exists an analytical solution $\tau^* = 0.25T$ for a harmonic signal, as derived in Reference (Michalowicz et al. 2009) for a discretized signal and summarized in Appendix I. This solution shows a good agreement with the τ^* value obtained from the analytical solution of the equation of motion presented in the last subsection.

VMDC ALGORITHM

The comparison of results in the previous section demonstrated that the MI test can be utilized to select τ^*. However, the online MI test strategy to select τ^* does not guarantee the stability condition $\tau|_{\max}$, and could lead to a sub-optimal performance for $\rho > \rho_{cr}$ because ρ_{cr} is assumed to be unknown. To ensure stability and produce better control performance when $\rho > \rho_{cr}$, the control gains $\mathbf{G}$ is allowed to be adaptive. In the upcoming subsection, the adaptive rule for the control gains is first derived, and the following subsection will present the online sequential adaptive algorithm of the VMDC.

Adaptive Control Gains

The back-propagation rule is used for adaptive control gains, where stability of system can be ensured using Lyapunov theory. The state-space representation of Eq. (2) is written

$$\dot{\mathbf{X}} = \mathbf{A}\mathbf{X} + \mathbf{B}_f f + \mathbf{B}_u u \tag{26}$$

with:

$$\mathbf{A} = \begin{bmatrix} 0 & 1 \\ -\frac{k}{m} & -\frac{c}{m} \end{bmatrix}_{2\times 2} \qquad \mathbf{X} = \begin{bmatrix} x \\ \dot{x} \end{bmatrix}_{2\times 1} \qquad \mathbf{B}_f = \mathbf{B}_u = \begin{bmatrix} 0 \\ -\frac{1}{m} \end{bmatrix}_{2\times 1}$$

where $\mathbf{X}$ is state vector and $u = \mathbf{G}^T \nu$ is control input (Eq. (1)) with adaptive gain $\mathbf{G} \in \mathbb{R}^{2\times 1}$, the observation $y(t) = x(t)$ and delay vector $\nu = [\ y(t) \quad y(t-\tau)\ ]^T \in \mathbb{R}^{2\times 1}$.

Take the following sliding surface s (Slotine et al. 1991)

$$s = \Lambda \mathbf{e} = \Lambda(\mathbf{X} - \mathbf{X}_d) = \Lambda \mathbf{X} \tag{27}$$

where $\Lambda = [\ 1 \quad \lambda\ ] \in \mathbb{R}^{1\times 2}$ is a user-defined weight matrix with λ being a strictly positive constant, e is the error between the actual state $\mathbf{X}$ and the desired state $\mathbf{X}_d$ taken as $\mathbf{X}_d = \mathbf{0}$, and consider the following Lyapunov function V

$$V = \frac{1}{2}[s^2 + \tilde{\mathbf{G}}^{\mathbf{T}} \Gamma^{-1} \tilde{\mathbf{G}}] \tag{28}$$

where $\Gamma = \gamma \mathbf{I}$ is positive definite diagonal matrix with equal weights γ representing the adaptation weights, and the tilde denotes the error between the desired and actual values ($\tilde{\mathbf{G}} = \mathbf{G} - \mathbf{G}_d$; $\tilde{\nu} = \nu - \nu_d$, with subscript d denoting the desired value). The time derivative $\dot{V}$ is given by

$$
\begin{aligned}
\dot{V} &= s\dot{s} + \tilde{\mathbf{G}}^T \Gamma^{-1} \dot{\tilde{\mathbf{G}}} \\
&= s\Lambda(\mathbf{A}\mathbf{e} + \mathbf{B}_u(\mathbf{G}^T \nu - \mathbf{G}_d^T \nu_d)) + \tilde{\mathbf{G}}^T \Gamma^{-1} \dot{\tilde{\mathbf{G}}} \\
&= s\Lambda(\mathbf{A}\mathbf{e} + \mathbf{B}_u(\tilde{\mathbf{G}}^T \nu + \mathbf{G}_d^T \nu - \mathbf{G}_d^T \nu_d)) + \tilde{\mathbf{G}}^T \Gamma^{-1} \dot{\tilde{\mathbf{G}}} \\
&= \mathbf{e}^T \Lambda^T \Lambda \mathbf{A}\mathbf{e} + \tilde{\mathbf{G}}^T \nu \Lambda \mathbf{B}_u s + \tilde{\mathbf{G}}^T \Gamma^{-1} \dot{\tilde{\mathbf{G}}} + s\Lambda \mathbf{B}_u \mathbf{G}_d^T \tilde{\nu} \\
&= \mathbf{e}^T \Lambda^T \Lambda \mathbf{A}\mathbf{e} + \tilde{\mathbf{G}}^T (\nu \Lambda \mathbf{B}_u s + \Gamma^{-1} \dot{\mathbf{G}}) + s\Lambda \mathbf{B}_u \mathbf{G}_d^T \tilde{\nu}
\end{aligned}
\tag{29}
$$

Substituting the following adaptation rule in Eq. (29)

$$
\dot{\mathbf{G}} = -\Gamma \nu \Lambda \hat{\mathbf{B}}_u s \tag{30}
$$

results the expression

$$
\dot{V} = \mathbf{e}^T \Lambda^T \Lambda \mathbf{A}\mathbf{e} + s\tilde{\mathbf{G}}^T \nu (\Lambda \mathbf{B}_u - \Lambda \hat{\mathbf{B}}_u) + s\Lambda \mathbf{B}_u \mathbf{G}_d^T \tilde{\nu} \tag{31}
$$

where $\hat{\mathbf{B}}_u$ is an estimation of vector $\mathbf{B}_u$, with $\mathbf{B}_u$ comprising knowledge of mass parameters only, which estimation can be relatively straightforward. The first term in Eq. (31) is negative definite for $\mathbf{A}$ negative definite, as it is the case in most applications to structural control (Laflamme et al. 2012a). The second term is assumed close to zero with $\Lambda \hat{\mathbf{B}}_u \approx \Lambda \mathbf{B}_u$. The last term is neglected because it is assumed that the delay vector will converge to $\tilde{\nu}_d$ ($\tilde{\nu} \approx \mathbf{0}$). It results that Eq. (31) is overall negative definite, and the state $\mathbf{X}$ will converge to 0.

Lastly, the discrete form of the adaptation rule (Eq. (30) is written

$$
\mathbf{G}(t) = \mathbf{G}(t-1) - \Delta_t \Gamma \nu \Lambda \hat{\mathbf{B}}_u s \tag{32}
$$

Adaptive Time Delay

A prior strategy in Refs. (Laflamme et al. 2011; Cao and Laflamme 2016a) was to compute the optimal time delay τ^* using the MI test continuously, at each time step. While successful, this technique resulted in high computational time, which may impede real-time applicability of the algorithm. Instead, τ^* is now computed at discrete time intervals, at every n steps, and kept constant over that time interval. Note that the first time delay τ_1^* can be selected arbitrarily due to the lack of prior data. Once τ_i^* is computed, $\tau(t)$ is varied smoothly over a transition region using a C^∞ function of the following type (Laflamme et al. 2011) :

$$\beta(t) = \frac{1}{1 + e^{-\frac{\eta_1 (t - t_0(i) - \eta_2/2)}{\eta_2}}} \tag{33}$$

where t_0 is the start time of the ith time interval, and η_1 and η_2 are constants with η_2 representing the width of the transition region. The adaptive time delay $\tau(t)$ is taken as

$$\tau(t) = (1 - \beta(t))\tau^*_{i-1} + \beta(t)\tau^*_i \tag{34}$$

where τ^*_{i-1} and τ^*_i are the computed optimal time delays at corresponding time intervals $i-1$ and i, respectively, and $\tau(t) \approx \tau^*_i$ for $\beta \gg 0$.

Sequential Adaptive VMDC Algorithm

In summary, the sequential application of the VMDC is as follows:

1. Determine if τ needs an update (every n steps); if not, jump to step 4.
2. Compute the probabilities p$(\cdot)$ based on the last n observations in $\mathbf{y}$ (Eq. (25)).
3. Find τ^* by conducting the MI test (Eq. (25)).
4. Adapt $\tau(t)$ using Eq. (34).
5. Construct $v(t)$.
6. Calculate the sliding surface error $\mathbf{s}$ (Eq. 27) and adapt $\mathbf{G}$ using Eq. (32).
7. Compute the output $u(t) = \mathbf{G}^T(t)v(t)$.

Note that step 2 is conducted by classifying the last n observations into a pre-defined number of bins $\mathrm{MI}_{\mathrm{bin}}$. In previous work (Laflamme et al. 2012a; Cao and Laflamme 2016a), the authors showed that the MI test could be applied in real-time provided that the search space for τ was limited over $[\ \tau(t-1) - \Delta_t \quad \tau(t-1) + \Delta_t\ ]$ for n not unrealistically large. Here, the search space is taken over the last n observations.

PARAMETRIC STUDY

This section conducts parametric studies to demonstrate the performance of the proposed VMDC. Numerical simulations are conducted on the SDOF system schematized in Fig. 5 subjected to a harmonic excitation $f(t) = \hat{f}\sin(\Omega t)$, and equipped with an ideal actuator (e.g., no delay) providing a force $u(t)$ bounded by $u_{\max}$. The simulation parameters for SDOF are listed in Table 1. The numerical algorithm follows the discrete form of a Duhamel integral involving the free vibration response (Connor and Laflamme 2014)

$$\mathbf{X}(t+1) = e^{\mathbf{A}\Delta_t}\mathbf{X}(t) + \mathbf{A}^{-1}(e^{\mathbf{A}\Delta_t} - \mathbf{I})[\mathbf{B}_f f(t) + \mathbf{B}_u u(t)] \tag{35}$$

with:

$$\mathbf{I} = \begin{bmatrix} 1 & 0 \\ 0 & 1 \end{bmatrix}_{2\times 2}$$

Observation Size

The effects of the observation size n (e.g., step size for the MI tests) on the performance of the VMDC is first investigated. The SDOF system (Fig. 5) is subjected to two different harmonic excitations: 1) $\Omega = 0.5\omega_n$, which is a frequency located in the zone governed by stability bounds on ρ_τ; and 2) $\Omega = 2\omega_n$, which is a zone of sub-optimal performance for $\rho_\tau > 0$. The control objective is displacement reduction. It is used to assess the performance of the VMDC.

The mitigation performance and normalized computation time under observation size $n \in [\ 200 \quad 2000\ ]$ are plotted in Fig. 6. The normalized computation time is the average computation time per simulation divided by the simulation time required for $n = 2000$. The performance of the VMDC increases with increasing n over the range $n = 200$ to $n = 1000$ for both excitations. After $n = 1200$, the performance starts decreasing with increasing n. This can be explained by the incorporation of different dynamics that occurred in the past, arising from the adaptive control formulation, and these different dynamics do not represent the current system behavior appropriately. The computation time increases approximately linearly with n due to the growing search space in the MI test.

Figure 7 are time series plots illustrating the VMDC's mitigation performance for three observation sizes: $n = 500$, $n = 1000$, and $n = 2000$. Figure 7 (a) and (b) compare the displacement responses for all three strategies under a low frequency excitation ($\Omega = 0.5\omega_n$) and a higher frequency excitation ($\Omega = 2\omega_n$), respectively. For $\Omega = 0.5\omega_n$, $n = 1000$ provides the best performance, as expected from Fig. 6, and both $n = 500$ and $n = 2000$ lead to more chattering after 7 s. For $\Omega = 2\omega_n$, $n = 500$ outperforms other strategies, also as expected, and this performance is attributed to the adaptation of ρ_τ occurring rapidly, as shown in the evolution of ρ_τ plotted in Fig. 7(d). The extreme value $n = 2000$ shows to underperform under strategies, and does not appear to converge or oscillate around a particular value of ρ_τ for the low frequency excitation (Fig. 7(c)). From the simulation results in this section, a value of $n = 1000$ is selected for further simulations.

Adaptive Control Strategy

Different adaptive strategies are now considered in order to further evaluate the performance of the VMDC, in particular the effect of the adaptive rules on the control gains and adaptive time delay. The adaptive strategies under investigation are:

1. The proposed VMDC.
2. Fixed gains & adaptive delay: Control gains are taken as $\rho_{g1} = 2$ and $\rho_{g2} = -1$, which are the same values as used to create Fig. 1. The time delay is variable as per the VMDC algorithm.
3. Adaptive gain & fixed delay: Control gains are adapted as per the VMDC algorithm. The time delay is selected from Fig. 4.
4. Fixed gain & fixed delay: Control gains are taken as $\rho_{g1} = 2$ and $\rho_{g2} = -1$, and the time delay is selected from Fig. 4.

The maximum control force is bounded by $u_{\max}$ = 2 kN for each adaptive strategy. The displacement reduction under a harmonic excitation is plotted in Fig. 8 for various frequency ratios $\rho \in [\ 0.1 \quad 3\ ]$ under each control cases. Results show that proposed VMDC provides enhanced mitigation performance, specifically at frequency ratios $\rho > 1$ for which all the other control strategies quickly lead to increases in the SDOF's displacement, while the VMDC is still successful at reducing displacements. Of particular interest is the comparison of the VMDC performance with the adaptive gain & fixed delay strategies; the inclusion of a time-varying τ in the algorithm results in a significant gain in performance.

The time series responses of the SDOF system are plotted in Fig. 9 for $\Omega = 0.5\omega_n$ and $\Omega = 2\omega_n$, as done in the previous section. These responses include displacements (Figs. 9(a) and (b)), control forces (Figs. 9(c) and (d)), and evolution of τ (Figs. 9(e) and (f)). A study of the control forces shows that all controllers saturate at $u_{\max}$ in the case $\Omega = 2\omega_n$, where the VMDC provides better displacement mitigation for the same force output. This relationship is not observable for $\Omega = 0.5\omega_n$, where the control force arising from the VMDC is slightly higher than the other control forces. However, in this case, all forces are applied in the same phase. The time delays for the case $\Omega = 0.5\omega_n$ oscillate around $\rho_\tau = 0.09$, but the oscillation occurs out-of-phase between both control strategies at the end of the simulation. For the case $\Omega = 2\omega_n$, both strategies appear to slowly converge.

Robustness to Noise

The robustness of the VMDC algorithm with respect to noise is studied by adding Gaussian noise to the observations. The noise level ranges from 0% to 25% of the measurement. The displacement reductions for frequency ratios ρ = 0.5, 1.0, 1.5, 2.0, 2.5 and 3.0 are plotted in Fig. 10. Results show relatively stable performance as a function of noise, with the worst case scenario ($\rho = 2.0$) exhibiting a decrease in mitigation performance of approximately 20% over a 25% noise for all cases.

Performance versus Knowledge

The performance of the VMDC is compared against different types of controller based on different levels of system knowledge. Four control cases are considered, each bounded by $u_{\max}$ = 2 kN. They are listed in order of required level of knowledge on the system's dynamics:

1. The proposed VMDC (VMDC). The VMDC requires knowledge of displacement and velocity observations.
2. The proposed VMDC using analytical MI test solution from Eq. 46 (VMDC & MI). The VMDC & MI requires knowledge of displacement and velocity observations, and of the excitation frequency Ω.
3. No time delay control (NDC): A negative displacement feedback with a pre-tuned control gain $g_{\text{NDC}} = 7.66$ kN/m obtained from the linear quadratic regulator (LQR) method described below.

$$u(t) = -g_{\text{NDC}} x(t) \tag{36}$$

The NDC requires knowledge of displacement observation and dynamic parameters enabling pre-tuning.

4. Linear quadratic regulator control (LQR): An LQR controller optimized to minimize a performance index ψ

$$\psi = \frac{1}{2}\int_0^\infty (\mathbf{X}^T(t)\mathbf{Q}\mathbf{X}(t) + u(t)Ru(t))dt \tag{37}$$

with:

$$\mathbf{Q} = \begin{bmatrix} Q_d & 0 \\ 0 & Q_v \end{bmatrix}_{2\times 2}$$

where $\mathbf{Q}$ and R are weights. In this simulation, $Q_d = Q_v = 30$ and $R = 1$. The LQR requires knowledge of displacement and velocity observations, as well as dynamic parameters.

The displacement reduction for the same excitation frequency ratios as in the previous section is plotted in Fig. 11 under each control cases. Results show that the VMDC outperforms an optimal pure-displacement feedback controller (NDC), and that adding knowledge of the excitation frequency (VMDC & MI) slightly increases mitigation performance. Also, the controller with enhanced knowledge (LQR) significantly outperforms the data-based strategies.

The performance of each control strategies is further studied under two specific harmonic frequencies ($\Omega = 0.5\omega_n$ and $\Omega = 2\omega_n$). The time series responses of displacements are plotted in Figs. 12(a) and (b). The mitigation performance of the VMDC is worse than the VMDC & MI case, but better than the NDC case. The LQR strategy significantly outperforms all other strategies. Figures. 12(c) and (d) are plots of the control forces over the last seconds of the excitations. For the relatively higher frequency excitation ($\Omega = 2\omega_n$), the forces saturates under the VMDC, VMDC & MI, and NDC strategies, indicating a sub-performance of the adaptive mechanism.

APPLICATION ON THREE DOF SYSTEM

The proposed VMDC algorithm is simulated on a more realistic system to evaluate structural control applications. The system is a three-story building model presented in Dyke et al. (Dyke and Spencer 1997). The building is

equipped with an actuator located between ground and the first floor. It is modeled as a spring-dashpot-mass system, as schematized in Fig. 13, with the dynamic properties listed in Table 2 extracted from Ref. (Dyke and Spencer 1997). In Fig. 13, $x_i(t)$ is the displacement at floor i, $f_i(t)$ the corresponding applied external loading, $a(t)$ the applied external ground motion, and $u(t)$ the control force from the actuator. Simulations assume the availability at each floor of the acceleration, velocity, and displacement states from a single sensor, either through integration or differentiation of the observation. The term full-state (FS) refers to the utilization of observations from all three sensors (one per floor), while the term limited-state (LS) refers to the utilization of a single observation taken at a given floor.

Two performance indices are considered in the analysis of simulation results:

- Maximum interstory displacement reduction J_1

$$J_1 = \frac{\max_{t,i}|z_{i,\mathrm{unc}}(t)| - \max_{t,i}|z_{i,\mathrm{ctrl}}(t)|}{\max_{t,i}|z_{i,\mathrm{unc}}(t)|} \tag{38}$$

  where $z_i = x_i - x_{i-1}$ denotes the interstory displacement at floor i, except at the first floor were $z_1 = x_1$, and subscripts unc and ctrl denote the uncontrolled and controlled states, respectively.

- Maximum acceleration reduction J_2

$$J_2 = \frac{\max_{t,i}|\ddot{x}_{i,\mathrm{unc}}(t)| - \max_{t,i}|\ddot{x}_{i,\mathrm{ctrl}}(t)|}{\max_{t,i}|\ddot{x}_{i,\mathrm{unc}}(t)|} \tag{39}$$

  where $\ddot{x}_i$ denotes the acceleration at floor i.

The performance of the VMDC is compared against two different LQR controllers with control weights

$$\mathbf{Q} = \begin{bmatrix} Q_d\mathbf{E} & \mathbf{0} \\ \mathbf{0} & Q_v\mathbf{E} \end{bmatrix}_{6\times 6}$$

with:

$$\mathbf{E} = \begin{bmatrix} E_1 & 0 & 0 \\ 0 & E_2 & 0 \\ 0 & 0 & E_3 \end{bmatrix}_{3\times 3}$$

where $\mathbf{E}$ is a diagonal matrix representing sensor location, with a value $E_{i,i} = 1$ when the sensor at floor i is available, and $E_{i,i} = 0$ when the sensor at floor i is unavailable.

One LQR controller assumes FS measurements (LQR-FS) with all three sensors available, and one LQR controller assumes LS measurements (LQR-LS) with only one sensor available. Two LQR-LS cases are considered: 1) only sensor 1 available; and 2) only sensor 3 available. A voltage delay is introduced in the actuator such that

$$\dot{u}_{\text{act},i} = -u_{\text{delay}}(u_{\text{act},i} - u_{\text{req},i}) \tag{40}$$

where u_{delay} is a positive constant representing the control delay, $u_{\text{req},i}$ is the required control force directly calculated by the controller and $u_{\text{act},i}$ is the actual control force from the actuator. Here, the delay coefficient u_{delay} is assumed to be 200 s^{-1} to be consistent with previous simulations conducted in Ref. (Laflamme et al. 2012b).

Harmonic Ground Motion

To enforce the assumption that the system's response can be modeled using an embedding dimension $d = 2$, the first simulation is conducted under a harmonic ground motion of the type $a(t) = \hat{a}_g \sin(\Omega t)$, with amplitude $\hat{a}_g$ =9.8 m/s^2, over the excitation frequency ratio range $\rho = \Omega/\omega_n \in [\ 0.1 \quad 3\ ]$. In this simulation, LQR control weights $Q_d = Q_v = 1$ and $R = 2 \times 10^{-7}$ are selected from pre-tuning to provide the best control performance. The parameter values used for the VMDC are listed in Table 3. The observation size n for the VFCC is taken as 250 samples.

The control performance for the VMDC and LQR-LS strategies are plotted in Fig. 14, for sensor 1-only available (Fig. 14(a) and (b)), and for sensor 3-only available (Fig. 14(c) and (d)), with results compared against the LQR-FS case. Under sensor 1-only, which corresponds to the sensor located at the actuator's position, the VMDC's performance compares very well with the LQR-LS and LQR-FS for performance metric J_1, sometimes outperforming them. In particular, the VMDC succeeds at reducing interstorey drift at $\rho = 0.2$, while both LQRs are worsening the response. With sensor 1-only and performance metric J_2, the VMDC underperforms the LQRs, except at $\rho = 0.9$ and $\rho = 2.8$ where it provides better performance. The excitation ratio $\rho = 0.9$ and 2.8 are close to the system's first and second natural frequencies shifted by the added stiffness from the LQR control rule.

Under sensor 3-only, the J_1 index shows that the VMDC provides similar mitigation performance to the LQR-FS up to $\rho = 1$, after which its relative performance decreases. However, it is performing much better than the LQR-LS, which fails at reducing interstorey displacement for $\rho < 0.3$, and both controllers fail at reducing displacement for $\rho > 2.2$. A study of the J_2 performance index also shows an overall increase in mitigation performance from the VMDC compared with the LQR-LS, especially at relatively low ($\rho < 0.5$) and high frequencies ($\rho > 2.2$). The LQR-FS outperforms all controllers, except for $\rho = 0.9$ and $\rho = 2.8$, analogous to the sensor 1-only results.

A cross-comparison of results between available sensors show that both the VMDC and LQR-LS perform better when utilizing the observations from the sensor close to the actuator (sensor 1). Also, when considering limited sensors, the data-based VMDC controller appears to be a better strategy than the model-based LQR-LS controller, except for mitigating acceleration under the sensor 1-only available case.

Multi-Hazard Excitations

We further demonstrate the performance of the VMDC using realistic hazards on the 3DOF system shown in Fig. 13. These hazards consist of non-simultaneous high wind and seismic events. A 10 min wind speed time series data is simulated using a variable wind speed model and parameters used by authors in Ref. (Cao et al. 2016), but where the wind speed gust frequency is tuned to the first natural frequency of the 3-story building. Wind loads $f_i(t)$ on floor $i = 1,2,3$ are scaled to a maximum magnitude of 1 kN. The North-South component of the 1940 El Centro earthquake is used for the seismic load $a(t)$. The earthquake time scale is scaled down to be consistent with the model size, as done in Ref. (Dyke and Spencer 1997). The time history series of wind load and seismic excitation are plotted in Fig. 15. The LQR control weights are pre-tuned separately for different excitations to provide the best control performance. Under the wind load, $Q_d = Q_v = 1$ and $R = 2 \times 10^{-6}$ are selected. For the seismic load, $Q_d = Q_v = 1$ and $R = 7 \times 10^{-8}$ are used. An observation size of $n = 100$ for the VMDC is taken. While the embedding dimension d is kept at $d = 2$ for the wind excitation, it is taken at $d = 3$ for earthquake excitation given the higher level of chaos in the excitation.

Simulation results are listed in Table 4. The VMDC significantly performs the LQR-LS controller in every cases, which demonstrates the superiority of the VMDC when only limited measurements are utilized. It also outperforms or slightly underperforms the LQR-FS in all cases, except for the seismic excitation when only sensor 3 is used in the feedback loop for which the VMDC significantly underperforms the LQR-FS controller. This subperformance can be attributed to the lack of information present in sensor 3's measurements, which, unlike sensor 1, measures a filtered form of the seismic excitation. Such subperformance is also observed in the LQR-LS case. Generally, as observed previously, the reliance on a sensor located far from the actuator results in worst performance.

CONCLUSION

A novel data-driven controller, termed Variable Multi-Delay Controller (VMDC), has been presented. The VMDC has the particularly of being capable of adapting its input space to the dynamics of the excitation. This makes it a good candidate for multi-hazard mitigation, because it does not require different tuning parameters for different types of excitations. The VMDC specialises the input space adaptation to varying the time delay of the observations used as inputs, while keeping the dimension of the observations constant. In future work, the VMDC will be extended to be capable of simultaneously varying both the time delay and dimension of the input space, forming a more generalized input-space dependent controller.

Parametric studies were conducted to evaluate the performance of the VMDC. Results show that the performance is sensitive to the choice of the observation size used in the MI test, and a particular value was selected to conduct the remaining of the parametric studies. Further studies showed that the inclusion of an adaptive input space resulted in a significant gain in performance versus a constant input space strategies, and that the VMDC was robust with respect to noise. When compared with an optimal LQR controller, the VMDC performed similarly at low excitation frequency

ratios, but underperformed the LQR controller significantly for higher excitation frequency ratios, illustrating a critical difference in performance resulting from different levels of knowledge on the system's dynamics.

Additional simulations were conducted on a three degrees-of-freedom (DOF) structure equipped with a single actuator at the first floor. Simulations compared the performance of the VMDC based on limited-state feedback (e.g., a single sensor) with a full-state feedback LQR (LQR-FS) and a limited-state feedback LQR (LQR-LS). For the harmonic ground motion excitation, results show that the VMDC performed as well as the LQR-LS at mitigating displacement, whether the sensor providing feedback was located at the actuator's DOF or at another floor. The VMDC also performed similarly to the LQR-FS at displacement mitigation when the limited-state feedback was obtained at the actuator's DOF. Results from acceleration mitigation showed that the VMDC underperformed the LQR strategies when limited feedback was obtained at the actuator's DOF, and outperformed the LQR-LS when limited-state feedback was obtained from another floor. Overall, the VMDC performed better when the limited-state feedback was obtained from the actuator's DOF. Further simulations were conducted on the 3DOF system exposed to two realistic non-simultaneous excitations - wind and seismic. Results were similar to that of the harmonic ground motion study.

Results presented in this paper demonstrated the ability of the controller at providing great mitigation performance based on limited knowledge and limited feedback from the system. It is therefore a great candidate at multi-hazard applications, because it 1) utilizes local and limited measurements only; 2) does not require prior evaluation or training; 3) is capable of extracting key features from unknown excitation; and 4) adapts to systems nonstationarities.

ACKNOWLEDGMENT

This material is based upon work supported by the National Science Foundation under Grant No. 1300960. Their support is gratefully acknowledged. Any opinions, findings, and conclusions or recommendations expressed in this material are those of the authors and do not necessarily reflect the views of the National Science Foundation.

REFERENCES

Amjadian, M. and Agrawal, A. K. (2017). "Vibration control using a variable coil-based friction damper." SPIE Smart Structures and Materials+ Nondestructive Evaluation and Health Monitoring, International Society for Optics and Photonics, 101642J–101642J.

Anderson, B. D. and Dehghani, A. (2008). "Challenges of adaptive control–past, permanent and future." Annual reviews in control, 32(2), 123–135.

Anderson, B. D. et al.(2005). "Failures of adaptive control theory and their resolution." Communications in Information & Systems, 5(1), 1–20.

Caballero, V. (2000). "On an embedding theorem." Acta Mathematica Hungarica, 88(4), 269–278.

Campestrini, L., Eckhard, D., Gevers, M., and Bazanella, A. S. (2011). "Virtual reference feedback tuning for non-minimum phase plants." Automatica, 47(8), 1778–1784.

Cao, L., Downey, A., Laflamme, S., Taylor, D., and Ricles, J. (2015). "Variable friction device for structural control based on duo-servo vehicle brake: Modeling and experimental validation." Journal of Sound and Vibration, 348, 41–56.

Cao, L. and Laflamme, S. (2016a). "Input space-dependent controller for multi-hazard mitigation." SPIE Smart Structures and Materials+ Nondestructive Evaluation and Health Monitoring, 97992H–97992H.

Cao, L. and Laflamme, S. (2016b). "Multi-delay controller for multi-hazard mitigation." 2016 American Control Conference (ACC), 1851–1856.

Cao, L., Laflamme, S., Taylor, D., and Ricles, J. (2016). "Simulations of a variable friction device for multihazard mitigation." Journal of Structural Engineering, H4016001.

Connor, J. J. and Laflamme, S. (2014). Structural Motion Engineering. Springer.

Da Silva, A., Alexandre, P., Ferreira, V., and Velasquez, R. (2008). "Input space to neural network based load forecasters." International Journal of Forecasting, 24(4), 616–629.

Dyke, S. and Spencer, B. (1997). "A comparison of semi-active control strategies for the mr damper." Intelligent Information Systems, 1997. IIS'97. Proceedings, 580–584.

Fraser, A. M. and Swinney, H. L. (1986). "Independent coordinates for strange attractors from mutual information." Physical review A, 33(2), 1134.

Hou, Z. and Jin, S. (2011). "Data-driven model-free adaptive control for a class of mimo nonlinear discrete-time systems." Neural Networks, IEEE Transactions on, 22(12), 2173–2188.

Kennel, M., Brown, R., and Abarbanel, H. (1992). "Determining embedding dimension for phase-space reconstruction using a geometrical construction." Physical Review A, 45(6), 3403–3411.

Laflamme, S. and Connor, J. (2009). "Application of self-tuning Gaussian networks for control of civil structures equipped with magnetorheological dampers." Proceedings of SPIE, Vol. 7288, 72880M.

Laflamme, S., Slotine, J. E., and Connor, J. (2012a). "Self-organizing input space for control of structures." Smart Materials and Structures, 21(11), 115015.

Laflamme, S., Slotine, J.-J. E., and Connor, J. J. (2011). "Wavelet network for semi-active control." Journal of Engineering Mechanics.

Laflamme, S., Taylor, D., Abdellaoui Maane, M., and Connor, J. J. (2012b). "Modified friction device for control of large-scale systems." Structural control and health monitoring, 19(4), 548–564.

Lee, H.-J., Yang, G., Jung, H.-J., Spencer, B. F., and Lee, I.-W. (2006). "Semi-active neurocontrol of a base-isolated benchmark structure." Structural Control and Health Monitoring, 13(2-3), 682–692.

Li, H., Liu, H., Gao, H., and Shi, P. (2012). "Reliable fuzzy control for active suspension systems with actuator delay and fault." Fuzzy Systems, IEEE Transactions on, 20(2), 342–357.

Li, K. and Peng, J. (2007). "Neural input selection–A fast model-based approach." Neurocomputing, 70(4-6), 762–

769.

Love, J., Tait, M., and Toopchi-Nezhad, H. (2011). "A hybrid structural control system using a tuned liquid damper to reduce the wind induced motion of a base isolated structure." Engineering Structures, 33(3), 738–746.

Materazzi, A. L. and Ubertini, F. (2012). "Robust structural control with system constraints." Structural Control and Health Monitoring, 19(3), 472–490.

Michalowicz, J. V., Nichols, J. M., and Bucholtz, F. (2009). "Calculation of entropy and mutual information for sinusoids." Report no., DTIC Document.

Moniz, L., Nichols, J., Nichols, C., Seaver, M., Trickey, S., Todd, M., Pecora, L., and Virgin, L. (2005). "A multivariate, attractor-based approach to structural health monitoring." Journal of Sound and Vibration, 283(1-2), 295–310.

Monroig, E., Aihara, K., and Fujino, Y. (2009). "Modeling dynamics from only output data." Physical Review E, 79(5), 56208.

Overbey, L., Olson, C., and Todd, M. (2007). "A parametric investigation of state-space-based prediction error methods with stochastic excitation for structural health monitoring." Smart Materials and Structures, 16, 1621–1638.

Slotine, J.-J. E., Li, W., et al.(1991). Applied nonlinear control, Vol. 199. Prentice-hall Englewood Cliffs, NJ.

Spall, J. C. (2009). "Feedback and weighting mechanisms for improving jacobian estimates in the adaptive simultaneous perturbation algorithm." Automatic Control, IEEE Transactions on, 54(6), 1216–1229.

Stark, J. (1999). "Delay embeddings for forced systems. I. Deterministic forcing." Journal of Nonlinear Science, 9(3), 255–332.

Stark, J., Broomhead, D., Davies, M., and Huke, J. (2003). "Delay embeddings for forced systems. II. Stochastic forcing." Journal of Nonlinear Science, 13(6), 519–577.

Takens, F. (1981). "Detecting strange attractors in turbulence." Dynamical systems and turbulence, Warwick 1980, Springer, 366–381.

Tikka, J. (2009). "Simultaneous input variable and basis function selection for RBF networks." Neurocomputing, 72(10-12), 2649–2658.

Ubertini, F. (2008). "Active feedback control for cable vibrations." Smart Structures and Systems, 4(4), 407–428.

Ubertini, F. and Materazzi, A. L. (2013). "Seismic response control of buildings with force saturation constraints." Smart Structures and Systems, 12(2), 157–179.

Van Helvoort, J., de Jager, B., and Steinbuch, M. (2007). "Direct data-driven recursive controller unfalsification with analytic update." Automatica, 43(12), 2034–2046.

Venanzi, I., Ubertini, F., and Materazzi, A. L. (2013). "Optimal design of an array of active tuned mass dampers for wind-exposed high-rise buildings." Structural Control and Health Monitoring, 20(6), 903–917.

Yang, J. N. and Agrawal, A. K. (2002). "Semi-active hybrid control systems for nonlinear buildings against near-field earthquakes." Engineering Structures, 24(3), 271–280.

Zolock, J. and Greif, R. (2009). “A Methodology for the Modeling of Forced Dynamical Systems From Time Series Measurements Using Time-Delay Neural Networks.” Journal of Vibration and Acoustics, 131, 011003.

Zou, Z., Bao, Y., Li, H., Spencer, B. F., and Ou, J. (2015). “Embedding compressive sensing-based data loss recovery algorithm into wireless smart sensors for structural health monitoring.” Sensors Journal, IEEE, 15(2), 797–808.

APPENDIX I. OPTIMAL TIME DELAY FOR A HARMONIC SIGNAL BASED ON INFORMATION THEORY

Consider two signals $f_1(t)$ and $f_2(t)$ that consist of two sinusoidal functions with a phase shift angle $\phi \in [0, 2\pi]$.

$$\begin{aligned} f_1 &= \hat{f}_1 \sin(\theta) \\ f_2 &= \hat{f}_2 \sin(\theta + \phi) \end{aligned} \tag{41}$$

where θ is assumed to be uniformly distributed over $[-\pi, \pi]$, and can be taken as $\theta = \Omega t$. The $\mathrm{MI}(f_1, f_2)$ for $f_1(t)$ and $f_2(t)$ is given by

$$\begin{aligned} \mathrm{MI}(f_1, f_2) &= (N-1) + \log_2(\frac{\pi \hat{f}_2}{2}) - J(f_2|f_1) \\ J(f_2|f_1) &= \int_{-\hat{f}_1}^{\hat{f}_1} \frac{1}{\pi\sqrt{\hat{f}_1^2 - \alpha^2}} J(\mathrm{p}_\alpha) d\alpha \end{aligned} \tag{42}$$

where $J(\mathrm{p}_\alpha)$ is the discrete entropy, p_α is the discrete probability for a particular value α in f_1, and N is the length of the discretized signals. The discrete entropy $J(\mathrm{p}_\alpha)$ and probability p_α are given by

$$\begin{aligned} J(\mathrm{p}_\alpha) &= -\mathrm{p}_\alpha \log_2(\mathrm{p}_\alpha) - (1 - \mathrm{p}_\alpha)\log_2(1 - \mathrm{p}_\alpha) \\ \mathrm{p}_\alpha &= \frac{D_1}{D_1 + D_2} \end{aligned} \tag{43}$$

where D_1 and D_2 are defined by

$$\begin{aligned} D_1 &= \sqrt{\cos^2\phi + \frac{2\alpha}{\hat{f}_1}\sqrt{1 - (\frac{\alpha}{\hat{f}_1})^2}\sin\phi\cos\phi - (\frac{\alpha}{\hat{f}_1})^2\cos 2\phi} \\ D_2 &= \sqrt{\cos^2\phi - \frac{2\alpha}{\hat{f}_1}\sqrt{1 - (\frac{\alpha}{\hat{f}_1})^2}\sin\phi\cos\phi - (\frac{\alpha}{\hat{f}_1})^2\cos 2\phi} \end{aligned} \tag{44}$$

The first local minima of $\mathrm{MI}(f_1, f_2)$ can be detected when the discrete entropy $J(\mathrm{p}_\alpha)$ reaches its maximum value $J(\mathrm{p}_\alpha) = 1$. Therefore, the probability p_α will be 1/2 and the optimal phase shift ϕ_{opt}

$$\phi_{\mathrm{opt}} = \pm\frac{\pi}{2} \tag{45}$$

This is equivalent to a quarter of the excitation period 2π, or

$$\tau^* = 0.25T \tag{46}$$

FIGURE CAPTION LIST

Fig. 1: H function of an SDOF system using $\rho_{g1} = 2$, $\rho_{g2} = -1$, and $\rho_\tau = [0, 0.05, 0.15, 0.25]$.

Fig. 2: Stability condition of an SDOF system with damping ratio $\xi = 2\%$ and feedback coefficient $\rho_{g1} = 1$.

Fig. 3: Maximum time delay $\tau|_{\max}$ as a function of ρ_{g1} and ρ_{g2} for $\xi = 2\%$.

Fig. 4: Optimal time delay ratio ρ_τ subjected to different frequency input with $\rho_{g1} = 2$ and $\rho_{g2} = -1$.

Fig. 5: SDOF system.

Fig. 6: Maximum displacement reduction and normalized computation time versus observation size n: (a) $\Omega = 0.5\omega_n$; and (b) $\Omega = 2\omega_n$.

Fig. 7: Time series displacement response for various different observation size n : (a) $\Omega = 0.5\omega_n$; and (b) $\Omega = 2\omega_n$. Time series time delay for various observation size n : (c) $\Omega = 0.5\omega_n$; and (d) $\Omega = 2\omega_n$.

Fig. 8: Maximum displacement reductions under harmonic excitation as a function of ρ.

Fig. 9: Displacement responses: (a) $\Omega = 0.5\omega_n$; and (b) $\Omega = 2\omega_n$; control forces: (c) $\Omega = 0.5\omega_n$; and (d) $\Omega = 2\omega_n$; and time delays: (e) $\Omega = 0.5\omega_n$; and (f) $\Omega = 2\omega_n$.

Fig. 10: Maximum displacement reduction after stabilization with under various noise levels.

Fig. 11: Maximum displacement reductions after stabilization under different controllers.

Fig. 12: Simulation results for different control strategies: (a) displacement response, $\Omega = 0.5\omega_n$; and (b) displacement response, $\Omega = 2\omega_n$; (c) control forces over the last 5 seconds, $\Omega = 0.5\omega_n$; and (d) control forces over the last 2 seconds, $\Omega = 2\omega_n$.

Fig. 13: Three DOF equipped with a single actuator.

Fig. 14: Performance index under different control strategies and various frequency ratio ρ; sensor 1-only available (first floor): (a) J_1; and (b) J_2; sensor 3-only available (third and top floor): (c) J_1; and (d) J_2.

Fig. 15: Multi-hazard excitations: (a) A 10-minute duration of wind load time series; and (b) scaled time history series of the North-South component of the 1940 El Centro earthquake.

TABLE 1: Simulation parameters for SDOF

object	parameter class	parameter	value
model	natural period	T_n	1 s
	mass	m	0.05 kg
	stiffness	k	2 kN/m
	damping ratio	ξ	2%
input	sampling rate	Δ_t	0.001 s
	amplitude of excitation	$\hat{f}$	2 kN
	maximum force	$u_{\max}$	2 kN
	initial gain value	$g_1(t=0)$	4 kN/m
	initial gain value	$g_2(t=0)$	-2 kN/m
	discrete bin number	$\mathrm{MI}_{\mathrm{bin}}$	30
adaptation	learning rate	γ	1
	weight	λ	1
	weight	η_1	20
	weight	η_2	n/6

TABLE 2: Dynamic properties of the 3DOF structure

floor	mass (kg)	stiffness (N/m)	damping (N·s/m)
3	98.3	684000	50
2	98.3	684000	50
1	98.3	516000	125

TABLE 3: VMDC parameters

object	parameter class	parameter	value
input	maximum force	$u_{\max}$	1 kN
	initial gain value	$g_1(t=0)$	600 kN/m
	initial gain value	$g_2(t=0)$	-300 kN/m
	sampling rate	Δ_t	0.004 s
	discrete bin number	$\mathrm{MI}_{\mathrm{bin}}$	30
adaptation	observation size	n	250
	weight	λ	1
	learning rate	γ	1
	weight	η_1	20
	weight	η_2	160

TABLE 4: Performance index under multi-hazard excitations

	wind excitation				seismic excitation			
	sensor 1-only		sensor 3-only		sensor 1-only		sensor 3-only	
control case	J_1	J_2	J_1	J_2	J_1	J_2	J_1	J_2
VMDC	40.52	55.64	34.52	54.03	63.03	53.32	30.08	23.02
LQR-LS	31.45	44.68	29.28	38.85	58.33	45.48	24.69	5.63
LQR-FS	31.54	60.62	31.54	60.62	69.49	49.39	69.49	49.39

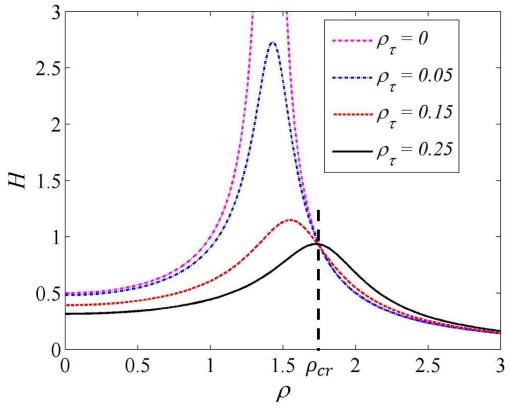

FIG. 1: H function of an SDOF system using $\rho_{g1} = 2$, $\rho_{g2} = -1$, and $\rho_\tau = [0, 0.05, 0.15, 0.25]$.

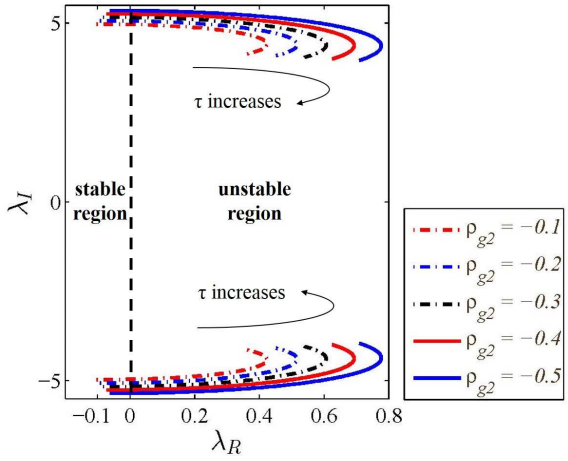

FIG. 2: Stability condition of an SDOF system with damping ratio $\xi = 2\%$ and feedback coefficient $\rho_{g1} = 1$.

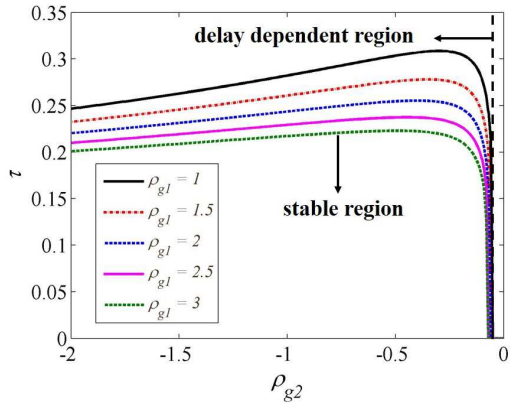

FIG. 3: Maximum time delay $\tau|_{\max}$ as a function of ρ_{g1} and ρ_{g2} for $\xi = 2\%$.

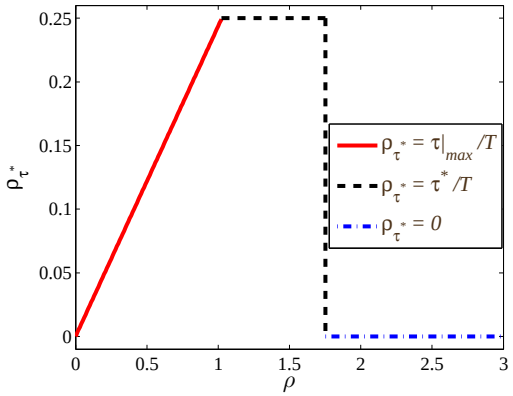

FIG. 4: Optimal time delay ratio ρ_τ subjected to different frequency input with $\rho_{g1} = 2$ and $\rho_{g2} = -1$.

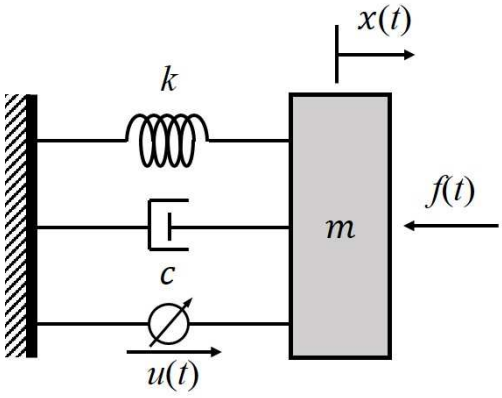

FIG. 5: SDOF system.

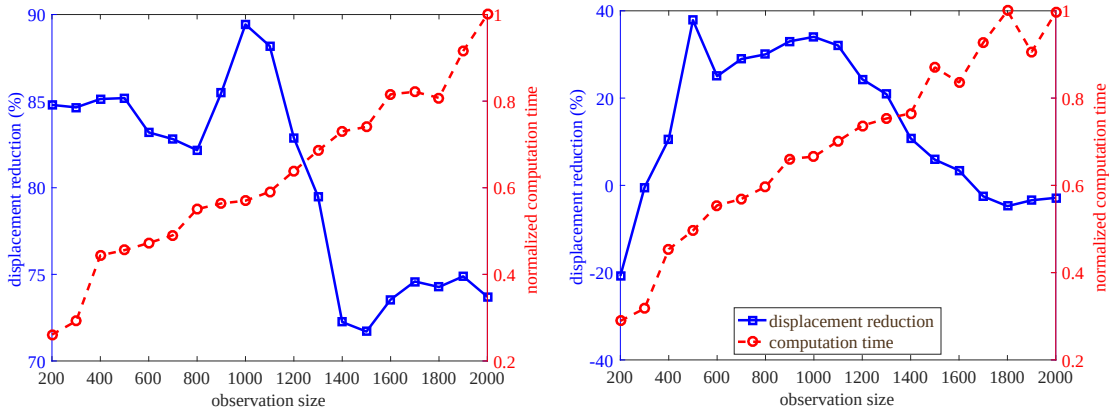

(a) (b)

FIG. 6: Maximum displacement reduction and normalized computation time versus observation size n: (a) $\Omega = 0.5\omega_n$; and (b) $\Omega = 2\omega_n$.

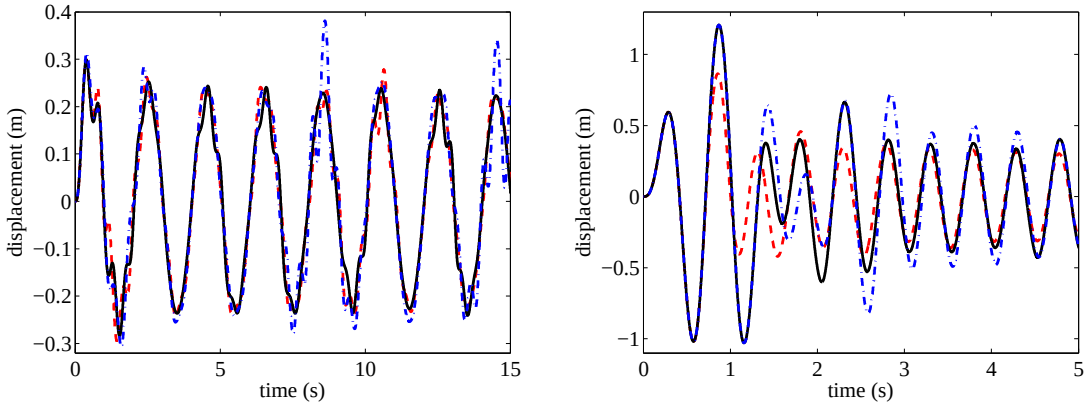

(a) (b)

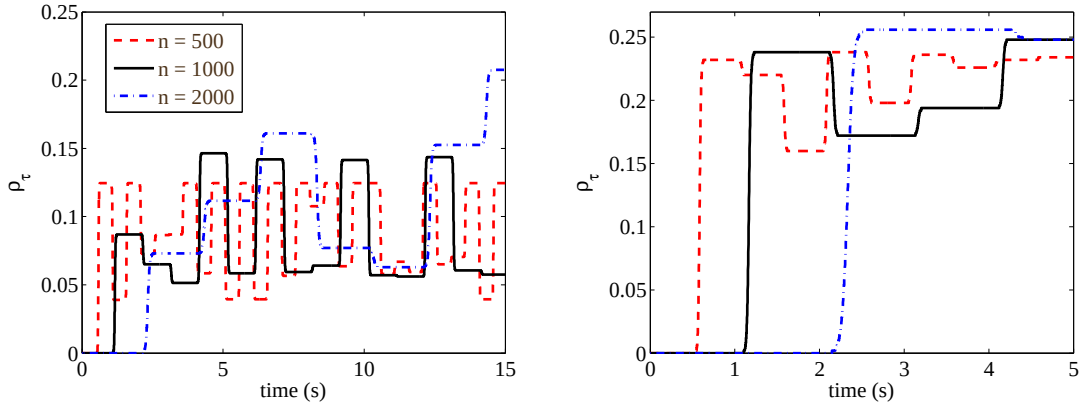

FIG. 7: Time series displacement response for various different observation size n : (a) $\Omega = 0.5\omega_n$; and (b) $\Omega = 2\omega_n$. Time series time delay for various observation size n : (c) $\Omega = 0.5\omega_n$; and (d) $\Omega = 2\omega_n$.

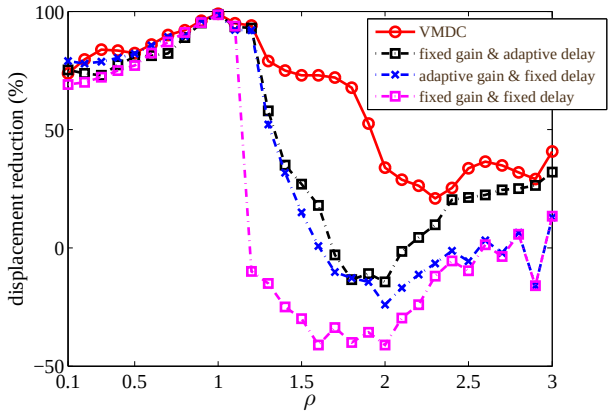

FIG. 8: Maximum displacement reductions under harmonic excitation as a function of ρ.

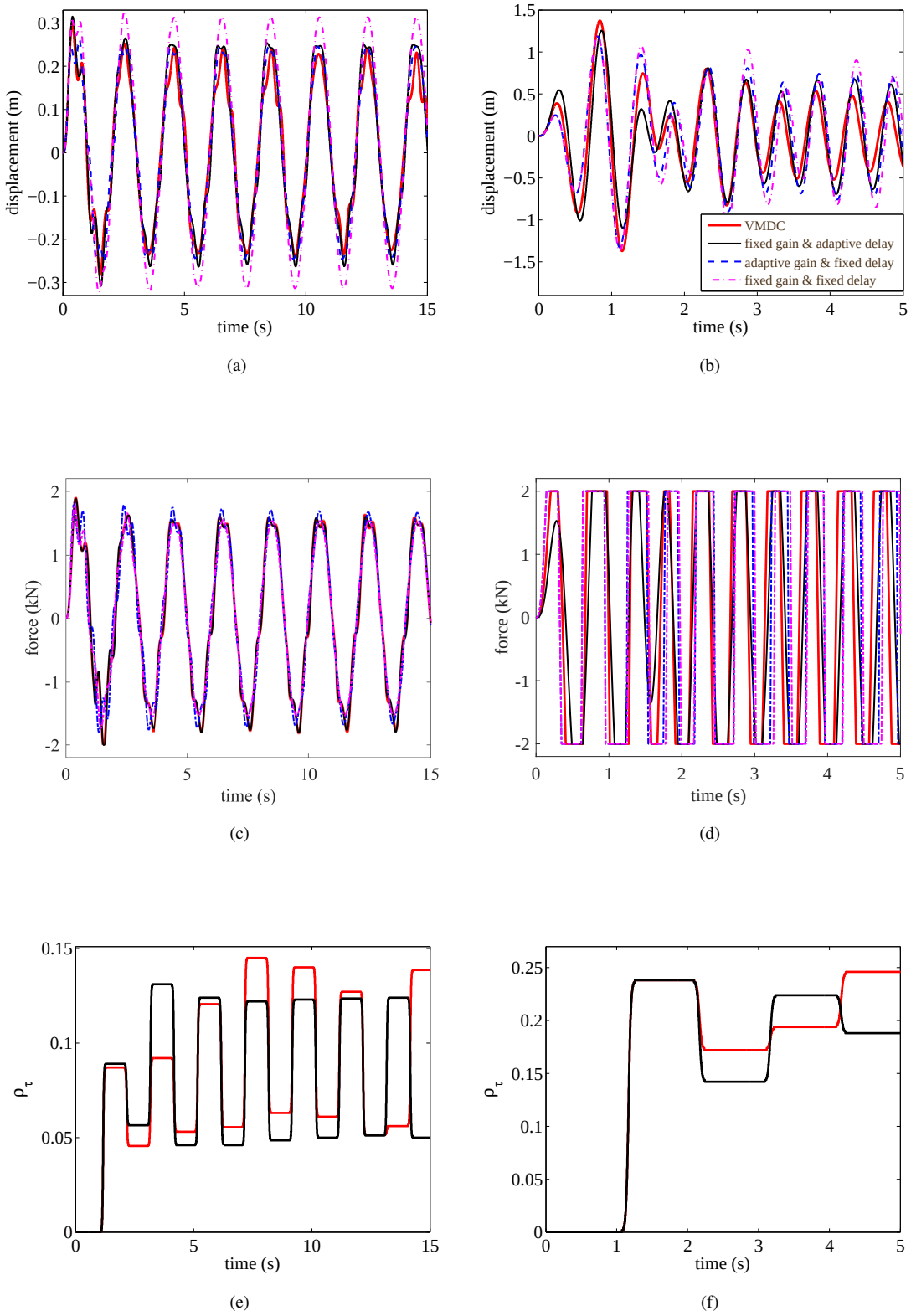

FIG. 9: Displacement responses: (a) $\Omega = 0.5\omega_n$; and (b) $\Omega = 2\omega_n$; control forces: (c) $\Omega = 0.5\omega_n$; and (d) $\Omega = 2\omega_n$; and time delays: (e) $\Omega = 0.5\omega_n$; and (f) $\Omega = 2\omega_n$.

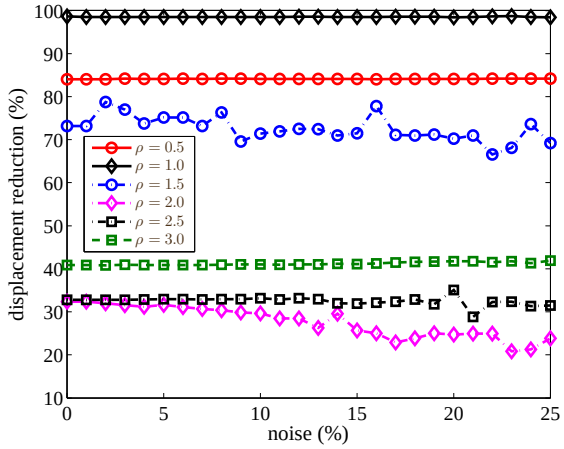

FIG. 10: Maximum displacement reduction after stabilization with under various noise levels.

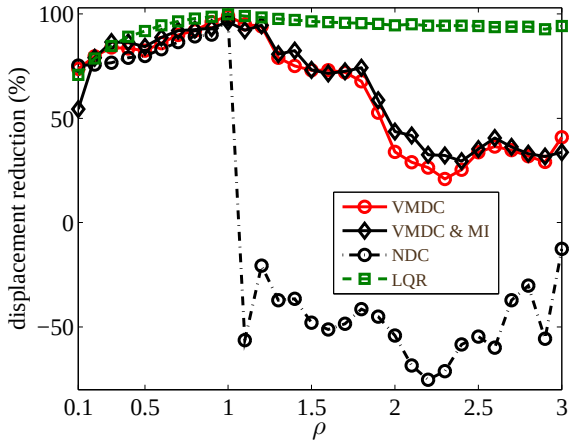

FIG. 11: Maximum displacement reductions after stabilization under different controllers.

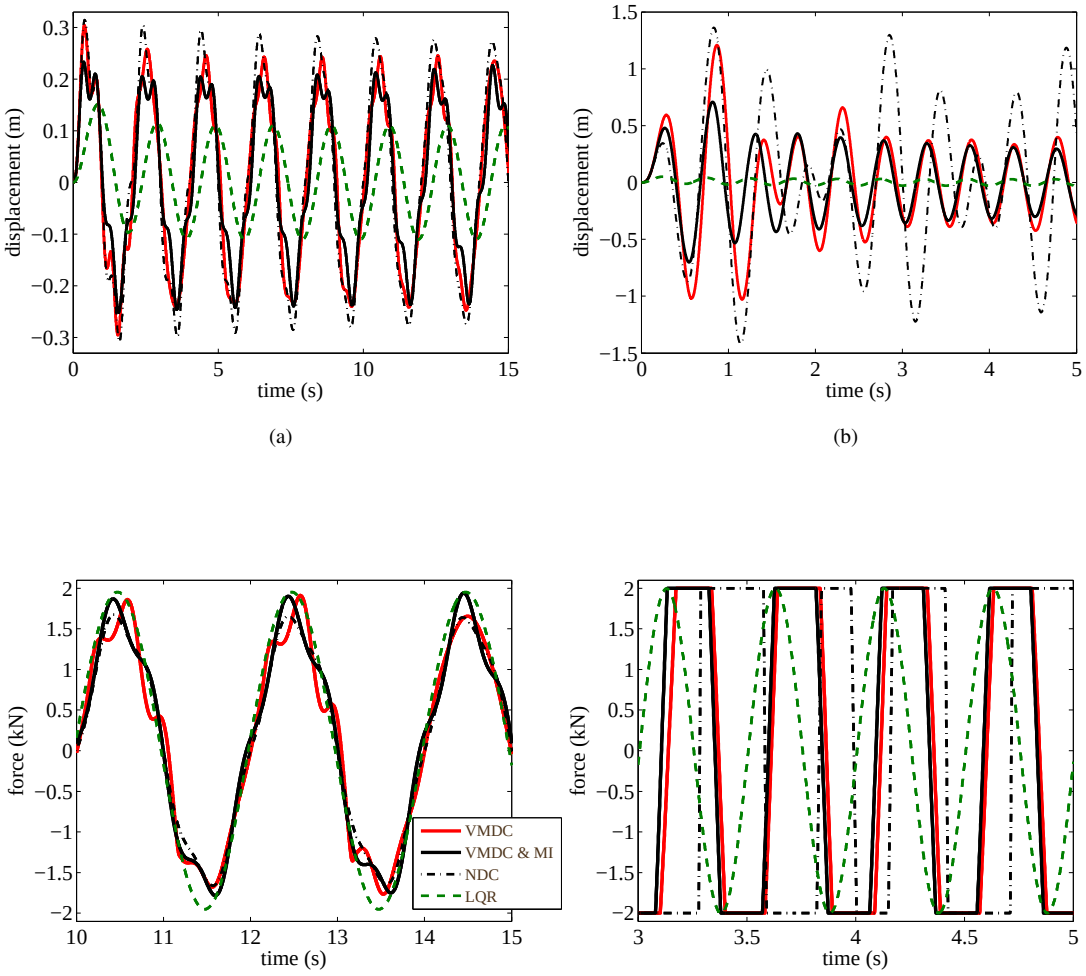

FIG. 12: Simulation results for different control strategies: (a) displacement response, $\Omega = 0.5\omega_n$; and (b) displacement response, $\Omega = 2\omega_n$; (c) control forces over the last 5 seconds, $\Omega = 0.5\omega_n$; and (d) control forces over the last 2 seconds, $\Omega = 2\omega_n$.

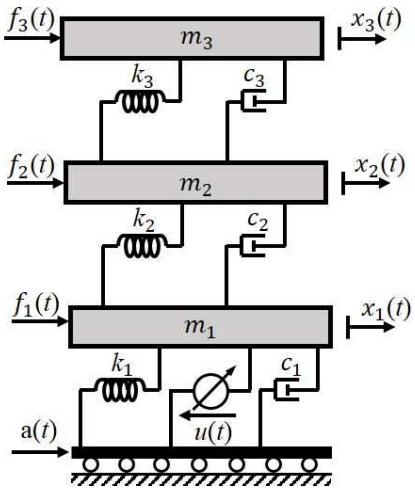

FIG. 13: Three DOF equipped with a single actuator.

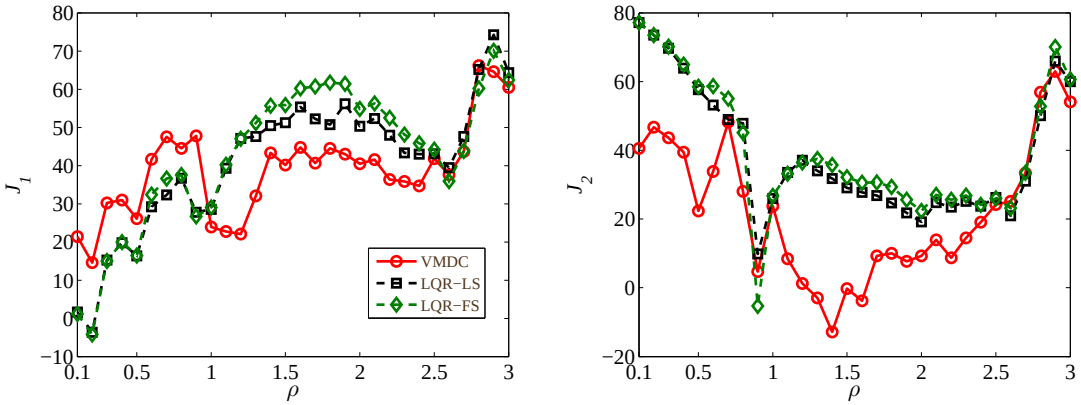

(a) (b)

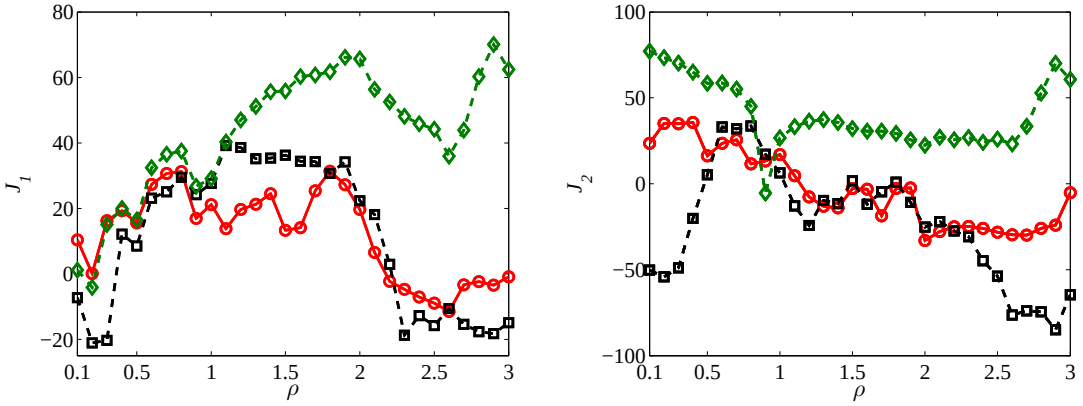

(c) (d)

FIG. 14: Performance index under different control strategies and various frequency ratio ρ; sensor 1-only available (first floor): (a) J_1; and (b) J_2; sensor 3-only available (third and top floor): (c) J_1; and (d) J_2.

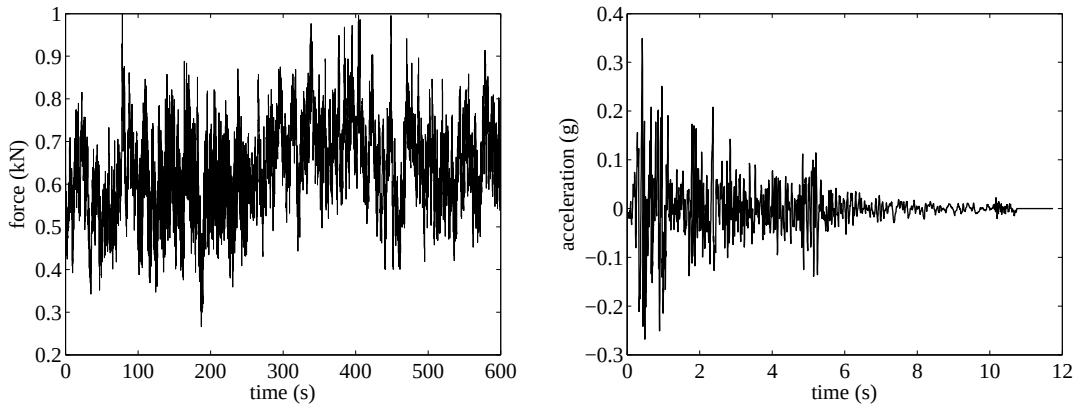

(a) (b)

FIG. 15: Multi-hazard excitations: (a) A 10-minute duration of wind load time series; and (b) scaled time history series of the North-South component of the 1940 El Centro earthquake